A Crystal Plasticity-Based Elasto-Viscoplastic Finite Element Model for Single Crystal Ice

Anantha Narayanan Suresh Babu (ananthsb@mit.edu)
2.073 Final Project: Fall 2024

1   Introduction

In recent years, the need for accurate simulation and prediction of rapidly evolving ice conditions has become increasingly apparent, emerging as one of the grand challenges of climate and marine sciences [15]. Since continuous satellite observations began in 1978, sea ice extent in the Arctic has been drastically reducing [18]. There is a growing consensus that an "ice-free" summer in the Arctic may occur in the next half-century, with a significant loss in the ice thickness and concentration [20]. Accurate and efficient ice forecasts are crucial for various stakeholders including local populations, scientists, and policy and decision-makers [26, 5].

Hence, it is abundantly clear that there is a need to accurately simulate the deformation of ice, over multiple scales in time and space. However, this is challenging since ice exhibits complex nonlinear material behavior and can exist in various forms than span length-scales of the order of millimeters (ice crystals) to several hundreds of kilometers (ice pancakes, floes, or sheets) each with vastly different dynamics [25, 12].

In the ice modeling community, there is still no consensus on the exact constitutive model or the exact rheological forms and associated parameters [21]. Ice sheets (length-scales of hundreds of kilometers) are typically simulated using continuum-based models that treat ice as a non-Newtonian fluid. These models assume a certain form of the yield criterion as a function of the stress invariants and typically assume a co-directional flow rule.

Some of the popular non-Newtonian models used in sea ice modeling are the simple Flato's cavitating fluid model [10] and other more complicated ones such as the ellipse [13], the teardrop, the lens, and the Mohr-Coulomb-ellipse based models [31]. Fig. 1 shows the yield curves of these models. More recently, some elasticity-based models have been developed to simulate the brittle behavior of ice [9]. However, there is still uncertainty over the validity of these models and whether they capture the true physics of ice.
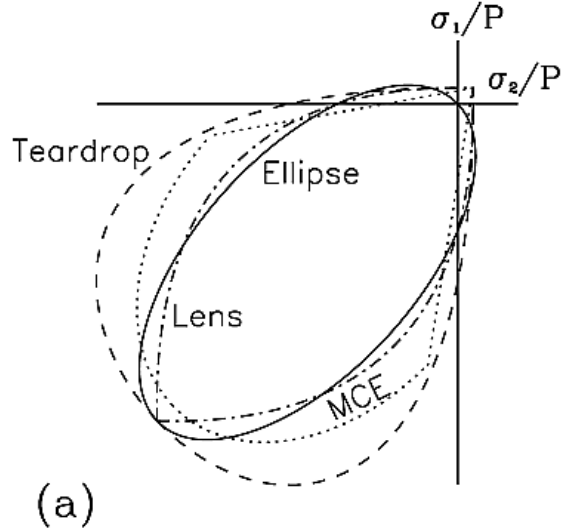
Figure 1: a) Yield curves of the popular non-Newtonian fluid-based models used to simulate large ice sheets of the scales of hundreds of kms. Source: [31]

Therefore, the following key questions motivate this project: 1) Can we develop a model grounded in the micro-mechanical principles of ice plasticity? 2) Is it possible to replace conventional normality-based flow rules with a more physically grounded alternative? 3) Can we develop a model capable of capturing the influence of crystal structure orientation on ice deformation?

To answer these questions, we focus on modeling a single crystal of ice to isolate the mechanical behavior and plastic deformation, i.e, our focus is now on the length-scales of a few micrometers to millimeters. Hence, we develop a crystal plasticity-based elasto-viscoplastic Finite Element Model for single crystal ice by adapting the works of [14, 3, 6]. The specific form of the model is inspired by the crystal structure and deformation mechanisms of ice.

To benchmark the results of the developed model, we compare numerical simulations from ABAQUS/Explicit against experiment results of uniaxial compression of single ice crystals from [29] and numerical results from [8].

2   Structure of Ice

First, we look at the crystal structure of ice. Fig. 2 shows the phase diagram of water. Ice has 21 possible crystal structures and 4 amorphous forms depending on the temperature and

pressure [19]. As snow, it has many physical structures depending on the temperature and water saturation [17]. Fig. 3 shows various physical forms and structures of snow.
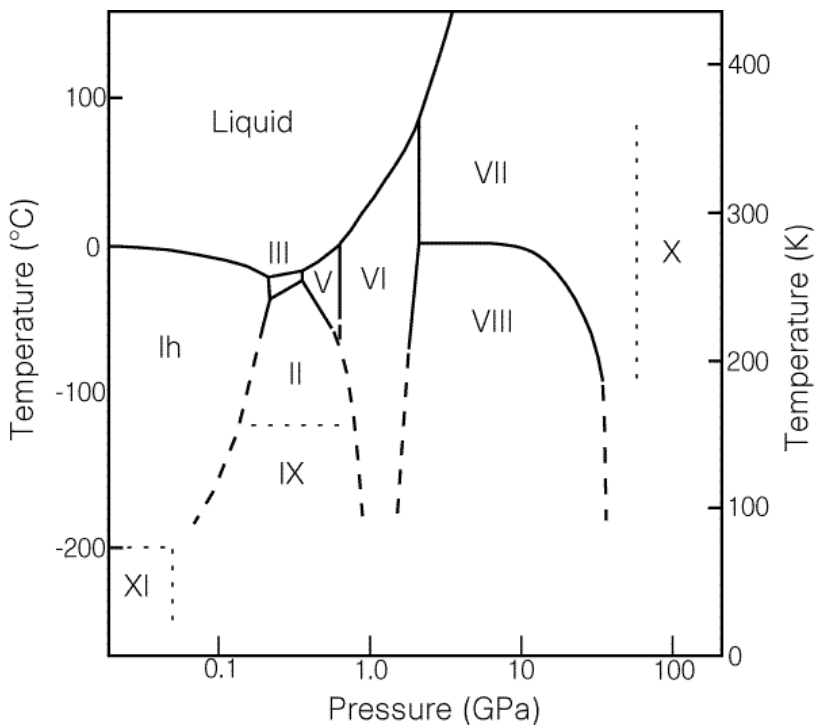

Figure 2: Phase diagram of water showing various crystalline forms of ice. Source: [19]

Many of the 21 crystal structures of ice are stable only at high pressures or under certain laboratory conditions. Ih ice is the most stable form of ice at the temperatures and pressures found on the Earth's surface, and is of predominant interest. Ih ice is formed by freezing water, another closely related variant, Ic ice, is formed by vapor deposition at extremely low temperatures and is not stable.

Ih ice has a hexagonal close-packed structure due to the presence of hydrogen bonding. Fig. 4 shows the lattice of ice with the basal plane, prismatic planes and orientation of the c-axis. The crystal lattice parameters are a = 0.4523 nm and c = 0.7367 nm. The c/a ratio (1.628) is very close to the ideal ratio (1.633) calculated using a hard sphere assumption. In Ih ice, both hydrogen and oxygen have very similar diffusion coefficients, and hence the lattice sites of oxygen are treated as the lattice sites of the Ih ice crystal [23].

Since we focus on Ih ice, our model is developed based on HCP crystal structure and the associated deformation mechanisms.
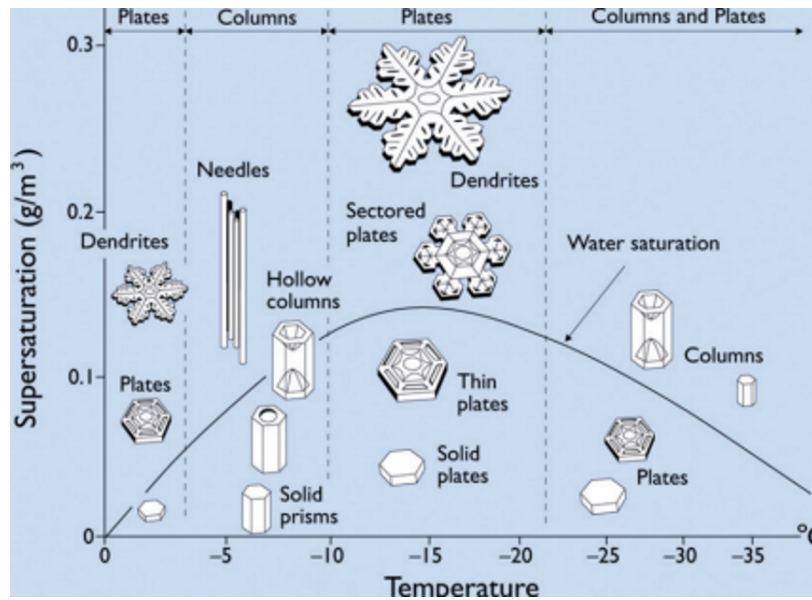
3

Figure 3: Morphology diagram of snow with temperature and water vapor supersaturation. Source: [17]
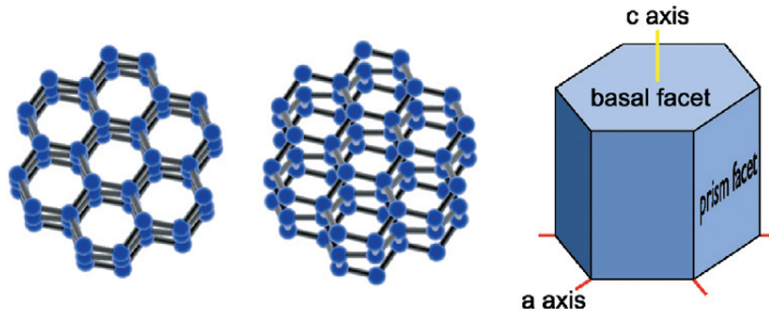

Figure 4: Left and Middle: Different views of "puckered" ice hexagons in the lattice, the balls represent oxygen atoms, and the bars represent hydrogen. Right: Schematic of HCP Ih ice showing the basal and prismatic faces, along with c- and a-axis orientation. Source: [17]

3 Deformation Mechanism of Ice

Next, we look at the deformation mechanism of ice and the associated micromechanical drivers of plasticity. The deformation of ice is significantly rate-dependent. Fig. 5 shows a schematic of the deformation of ice at various strain rates. At low strain rates, ice shows ductile behavior with strain softening. As the rate increases, the yield increases as expected. However, at a specific strain rate, ice undergoes ductile-to-brittle transition, after which it fails in a brittle fashion [23]. This motivates us to develop a rate-dependent viscoplastic model for ice. For this project, we focus on low strain rates to model the interesting strain softening behavior.
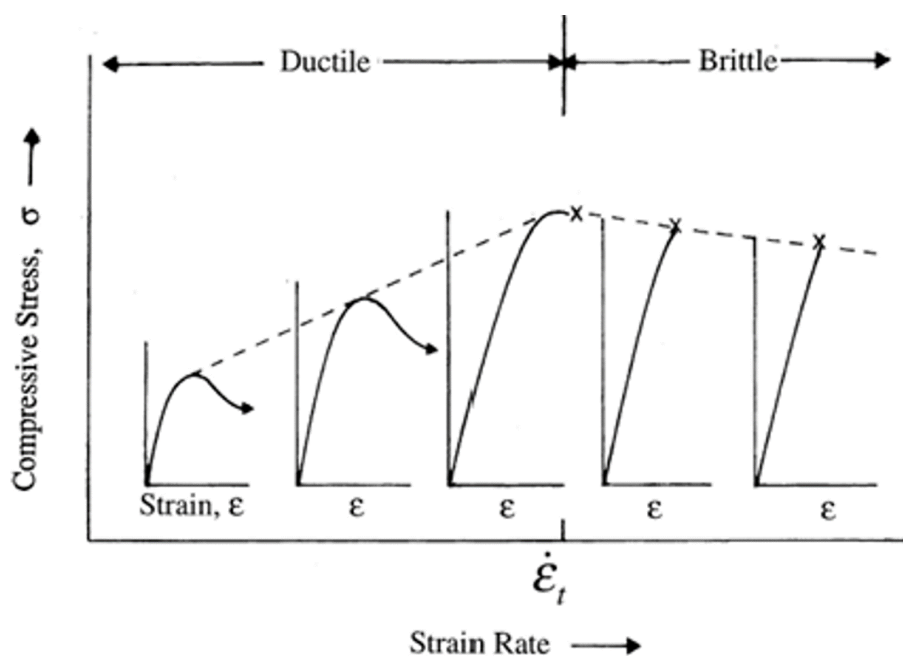

Figure 5: Schematic showing the strain-rate dependent uniaxial compressive behavior of ice. Source: [23]

For a typical HCP crystal, there are over 30 slip systems. Based on symmetry and orientation, they can be split into 5 groups: 3 systems of Basal $< a >$ slip, 3 systems of Prismatic $< a >$ slip, 6 systems of Pyramidal $< a >$ slip, 12 systems of 1st order Pyramidal $< c + a >$ slip and 6 systems of 2nd order pyramidal $< c + a >$ slip. Fig. 6 provides a sketch of the 30 slip systems. Basal slip systems are the preferred ones for plastic deformation since it contains a more densely packed system, followed by prismatic while pyramidal systems are the least densely packed. For Ih ice, it is enough to consider just the 3 systems of Basal $< a >$, 3

5

systems of Prismatic $< a >$ slip and 6 systems of 2nd order pyramidal $< c + a >$ slip to model its plastic deformation, leading to 12 active slip systems.
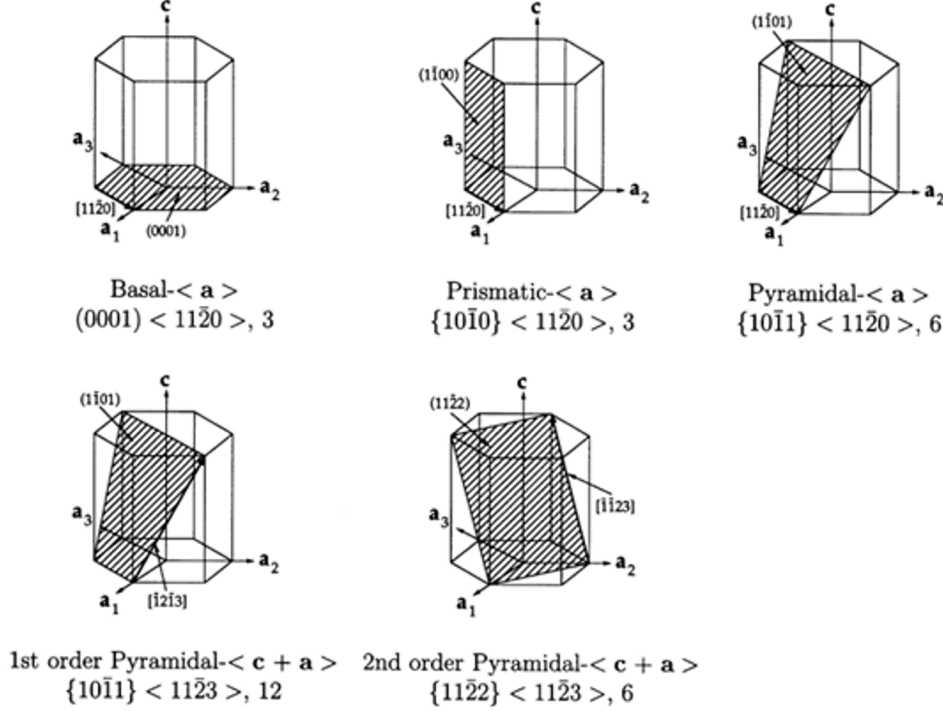

Figure 6: 5 groups of slip systems present in a typical HCP crystal. Source: [4]

Various experimental studies have been performed to study the deformation mechanism of single crystal ice (see [7] for more information). Typically, single crystal ice is cut from a bulk specimen grown using a seed. The reader is directed to [16] for additional details on growing single ice crystals. Uniaxial compression and shear experiments have shown that the main plastic deformation is dislocation slip, following Schmid's law [28]. Macroscopically, this leads to the shearing of the slip planes in the preferred slip direction. It has also been observed that single crystal ice shows stress softening when basal slip occurs and little-to-no hardening when non-basal slip occurs [22]. For Ih ice, basal slip systems are the preferred systems for shearing since they have the most closely packed structure. Hence, the crystal reorients itself during deformation to favor the basal systems.

Fig. 7 and Fig. 8 show the slip lines observed after uniaxial compression of a single ice crystal at different c-axis orientations. It can clearly be observed that the c-axis orientation of the ice crystal heavily influences the orientation of slip lines and the plastic deformation.
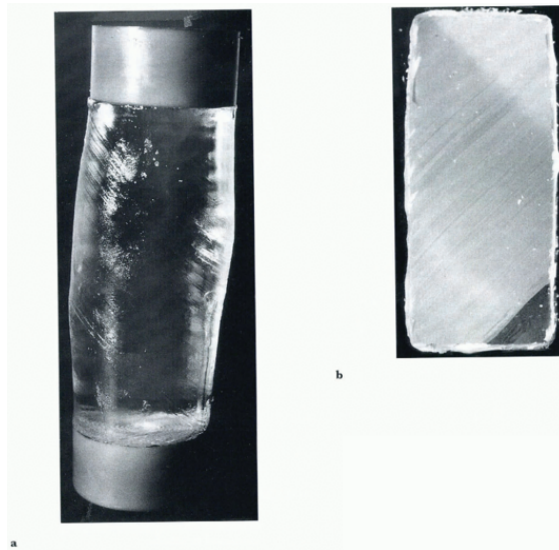
Figure 7: a) Slip lines observed during uniaxial compression of single ice crystal oriented at 45° b) Cross section showing clear slip lines. Source: [7]
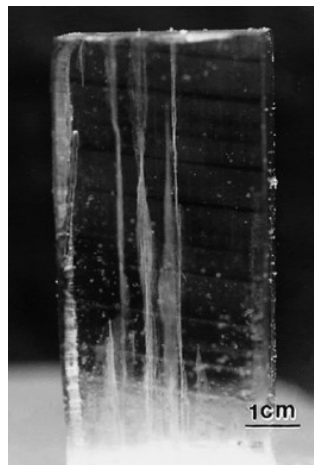

Figure 8: Slip lines observed during uniaxial compression of single ice crystal oriented at 5°. Source: [28]

Hence, the crystal structure, rate-dependent behavior, dislocation-slip-based deformation mechanism, and crystal orientation-dependent behavior of ice motivate us to develop a rate-dependent HCP crystal plasticity-based constitutive model.

4 Model Formulation

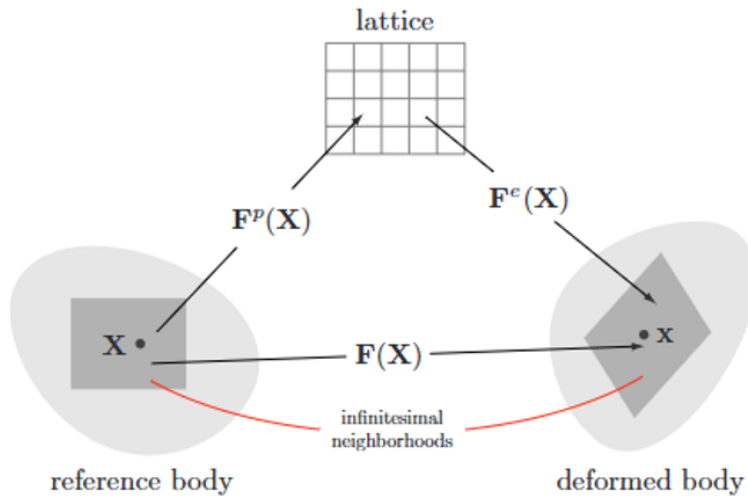To develop the crystal plasticity-based model, we follow the procedure illustrated in [6, 14, 3, 2].

Figure 9: Kroner decomposition showing the intermediate "lattice" state. Source: [2]

We use the Kröner decomposition to multiplicatively decompose the deformation gradient ($\mathbf{F}$) into an elastic part ($\mathbf{F}^e$) that represents the local stretching and rotation of the lattice and a plastic part ($\mathbf{F}^p$) that represents the plastic distortion due to the flow of defects (Fig. 9). The lattice refers to the intermediate structural space.

$$\mathbf{F} = \mathbf{F}^e \mathbf{F}^p \tag{1}$$

We assume plastic incompressibility, $\mathbf{F}^p = \mathbf{1}$ and $\det\mathbf{F}^e > 0$.

From the Kroner decomposition, the spatial velocity gradient ($\mathbf{L}$) can be obtained as

$$\mathbf{L} = \dot{\mathbf{F}}\mathbf{F}^{-1} = \dot{\mathbf{F}}^e\mathbf{F}^{e-1} + \mathbf{F}^e\mathbf{L}^p\mathbf{F}^{e-1} \tag{2}$$

Since ice undergoes small-to-moderate elastic deformations, we use the Green elastic strain measure defined as

$$\mathbf{E}^e = \frac{1}{2}\left(\mathbf{F}^{eT}\mathbf{F}^e - \mathbf{1}\right) \tag{3}$$

with associated second Piola-Kirchoff stress measure ($\mathbf{T}^*$) which is related to the Cauchy stress ($\mathbf{T}$) as

$$\mathbf{T}^* = \det(\mathbf{F}^e)\mathbf{F}^{e-1}\mathbf{T}(\mathbf{F}^e)^{-T} \tag{4}$$

The constitutive equation is defined to be linear

$$\mathbf{T}^* = \mathbb{C}\mathbf{E}^e \tag{5}$$

where $\mathbb{C}$ is the transversely anisotropic fourth-order elasticity tensor with 5 independent elastic constants. Transverse anisotropy is observed in most HCP crystals due to their distinct c-axis.

Next, we develop the flow rule. Since the dislocation motion occurs on the preferred slip systems, the plastic deformation gradient evolves as

$$\mathbf{L}^p = \dot{\mathbf{F}}^p\mathbf{F}^{p-1} = \sum_\alpha \dot{\gamma}^\alpha \mathbb{S}_0^\alpha \tag{6}$$

where $\mathbb{S}_0^\alpha$ is the Schmid tensor (a lattice tensor) of the slip system α defined using the slip directions (m_0^α) and the normals of the slip plane (n_0^α) as follows

$$\mathbb{S}_0^\alpha = m_0^\alpha \otimes n_0^\alpha \tag{7}$$

Thus, we have

$$\mathbf{L} = \mathbf{L}^e + \sum_\alpha \dot{\gamma}^\alpha \mathbf{F}^e \mathbb{S}_0^\alpha (\mathbf{F}^e)^{-1} \tag{8}$$

For Ih ice, there are 12 active slip systems and their slip directions and slip plane normals are provided below as shown in [4].

Since we are interested in the ductile plastic deformation of single crystal ice at -10° C, we use a simple power-law for the plastic shearing rate. We note that the power-law can

α	Miller-Bravais Notation	n_0^α	m_0^α
1	$(0001) < 11\bar{2}0 >$	0 0 1	$\frac{1}{2}\ \frac{-\sqrt{3}}{2}\ 0$
2	$(0001) < \bar{2}110 >$	0 0 1	$\frac{1}{2}\ \frac{\sqrt{3}}{2}\ 0$
3	$(0001) < 1\bar{2}10 >$	0 0 1	-1 0 0

Table 1: Basal $< a >$ Slip Systems $(0001) < 11\bar{2}0 >$

α	Miller-Bravais Notation	n_0^α	m_0^α
1	$(10\bar{1}0)[\bar{1}2\bar{1}0]$	0 1 0	1 0 0
2	$(01\bar{1}0)[\bar{2}110]$	$\frac{-\sqrt{3}}{2}\ \frac{1}{2}\ 0$	$\frac{1}{2}\ \frac{\sqrt{3}}{2}\ 0$
3	$(\bar{1}100)[\bar{1}\bar{1}20]$	$\frac{-\sqrt{3}}{2}\ -\frac{1}{2}\ 0$	$-\frac{1}{2}\ \frac{\sqrt{3}}{2}\ 0$

Table 2: Prismatic $< a >$ Slip Systems $\{10\bar{1}0\} < 11\bar{2}0 >$

α	Miller-Bravais Notation	n_0^α	m_0^α
1	$(11\bar{2}2)[\bar{1}\bar{1}23]$	$\frac{c}{2\sqrt{c^2+a^2}}\ \frac{-\sqrt{3}c}{2\sqrt{c^2+a^2}}\ \frac{a}{\sqrt{c^2+a^2}}$	$-\frac{a}{2\sqrt{c^2+a^2}}\ \frac{\sqrt{3}a}{2\sqrt{c^2+a^2}}\ \frac{c}{\sqrt{c^2+a^2}}$
2	$(\bar{1}2\bar{1}2)[1\bar{2}13]$	$\frac{c}{\sqrt{c^2+a^2}}\ 0\ \frac{a}{\sqrt{c^2+a^2}}$	$-\frac{a}{\sqrt{c^2+a^2}}\ 0\ \frac{c}{\sqrt{c^2+a^2}}$
3	$(\bar{2}112)[2\bar{1}\bar{1}3]$	$\frac{c}{2\sqrt{c^2+a^2}}\ \frac{\sqrt{3}c}{2\sqrt{c^2+a^2}}\ \frac{a}{\sqrt{c^2+a^2}}$	$-\frac{a}{2\sqrt{c^2+a^2}}\ \frac{-\sqrt{3}a}{2\sqrt{c^2+a^2}}\ \frac{c}{\sqrt{c^2+a^2}}$
4	$(\bar{1}\bar{1}22)[11\bar{2}3]$	$-\frac{c}{2\sqrt{c^2+a^2}}\ \frac{\sqrt{3}c}{2\sqrt{c^2+a^2}}\ \frac{a}{\sqrt{c^2+a^2}}$	$\frac{a}{2\sqrt{c^2+a^2}}\ -\frac{\sqrt{3}a}{2\sqrt{c^2+a^2}}\ \frac{c}{\sqrt{c^2+a^2}}$
5	$(1\bar{2}12)[\bar{1}2\bar{1}3]$	$-\frac{c}{\sqrt{c^2+a^2}}\ 0\ \frac{a}{\sqrt{c^2+a^2}}$	$\frac{a}{\sqrt{c^2+a^2}}\ 0\ \frac{c}{\sqrt{c^2+a^2}}$
6	$(2\bar{1}\bar{1}2)[\bar{2}113]$	$-\frac{c}{2\sqrt{c^2+a^2}}\ -\frac{\sqrt{3}c}{2\sqrt{c^2+a^2}}\ \frac{a}{\sqrt{c^2+a^2}}$	$\frac{a}{2\sqrt{c^2+a^2}}\ \frac{\sqrt{3}a}{2\sqrt{c^2+a^2}}\ \frac{c}{\sqrt{c^2+a^2}}$

Table 3: 2nd Order Pyramidal $\langle c + a \rangle$ Slip Systems $\{11\bar{2}2\} < 11\bar{2}3 >$

be modified to include the effects of temperature on ice deformation since it is based on a thermally activated Arrhenius-type form.

$$\dot{\gamma}^\alpha = \dot{\gamma}_0^\alpha \left| \frac{\tau^\alpha}{s^\alpha} \right|^{\frac{1}{m}} \text{sign}(\tau^\alpha) \tag{9}$$

where $\dot{\gamma}_0^\alpha$ is the reference slip rate, m is the rate sensitivity parameter and s^α is the slip resistance for the slip system α.

Finally, the slip resistance (s^α) is assumed to evolve as

$$\dot{s}^\alpha = \sum_\beta h_{\alpha\beta} \left| \dot{\gamma}^\beta \right| \tag{10}$$

where the evolution of the hardening moduli $(h_{\alpha\beta})$ are taken to follow [6].

$$h_{\alpha\beta} = H_{\alpha\beta}(s_{\text{sat}}^\alpha - s^\alpha) \tag{11}$$

Populating the hardening moduli is a cumbersome task since it could be as large as 900 parameters if we consider all 30 HCP slip systems. Hence, typically, the hardening moduli are assumed to be decomposed into a self-hardening component for co-planar slip systems and a latent-hardening component for non-co-planar slip systems [4]. For Ih ice, the effect of pyramidal systems is negligible on both co-planar and non-co-planar systems, hence, here we manually populate the $h_{\alpha\beta}$ parameters.

Finally, the equations are implemented in a VUMAT script in ABAQUS with the time integration procedure specified in [14].

5   Results and Applications

Next, we showcase applications of uniaxial compression of single-crystal ice at various strain rates and various crystal orientations (c-axis orientation).

5.1   Euler angles

First, we need to convert the crystal's c-axis orientation, or [hkil] notation coordinates to Euler angles, to be compatible with the developed VUMAT code. For this, we follow the procedure described in [1, 14] to get:

$$\phi = \arctan\left(\frac{-h}{k}\right)$$

$$\theta = \arccos\left(\frac{l}{\sqrt{h^2 + k^2 + l^2}}\right) \tag{12}$$

ω is indeterminate in this formulation, but can be safely set to 0 for our simulations. Since we are only interested in the c-axis orientation in this project, this can be achieved by just setting the value of the Euler angle θ to be the same as the crystal's c-axis rotation.

5.2 Parameter values

Parameter	Value
C_{11}	13930 MPa
C_{12}	7082 MPa
C_{13}	5765 MPa
C_{33}	15010 MPa
C_{44}	3014 MPa

Table 4: Transversely isotropic elastic parameters for HCP Ih ice

Slip system	s_0^α	s_{sat}^α	$\dot{\gamma}^\alpha$	m
Basal	0.035 MPa	0.008 MPa	10^{-6} /s	0.5
Prismatic	0.13 MPa	0.55 MPa	10^{-6} /s	0.35
Pyramidal	2.2 MPa	2.2 MPa	10^{-6} /s	0.25

Table 5: Plasticity parameters for HCP Ih ice

$H_{\alpha\beta}$	Basal	Prismatic	Pyramidal
Basal	70	125	0
Prismatic	125	110	0
Pyramidal	0	0	0

Table 6: Hardening matrix for HCP Ih ice

The parameter values that best describe the available data are shown in Tables 4, 5, and 6. The elastic parameters (Table 4) are taken from studies by [11, 8]. The hardening matrix

(Table 6) is taken from [27, 8]. The plasticity parameters (Table 5) were obtained by fitting the model with data from [8]. The parameter fitting strategy is described in the upcoming subsections.

We can observe that the slip resistance is the lowest along the basal planes, as expected from experiment studies since the basal planes are the most densely packed and are the most favorable systems for slip. The next least slip resistance is along the prismatic systems with the pyramidal systems having the most resistance ($\simeq$ 100 times more resistance than basal planes and $\simeq$ 10 times more resistance than prismatic planes). The values of m also suggest that Ih ice deformation is significantly rate-dependent as expected from experimental evidence.

5.3   ABAQUS Simulations

All simulations were carried out on a cube of side 1 mm under uniaxial compression. C3D8R mesh elements were used with hour-glass control. A VUMAT was used to run the simulations with ABAQUS/ Explicit. For the stress-strain curves, a MATLAB script was used to generate loading velocity profiles for the various strain rates.

5.3.1   Rate-dependence

First, we validate the model by comparing uniaxial compression simulations of a 45° c-axis oriented crystal at three different strain rates. The benchmark data taken from [8] is shown in Fig. 10. We can see that at 45° orientation, ice shows strain softening, and the yield peak increases rapidly as the strain rate increases. At larger strains, the stress curve converges to a stationary stress whose value increases with increasing strain rate.

The results of the developed model are shown in Fig. 11. Our developed rate-dependent model shows good qualitative and quantitative agreement compared to the benchmark shown in Fig. 10.

5.3.2   Lattice rotation/ c-axis reorientation

Next, from experimental results, it can be seen that the ice crystal reorients itself during compression to favor the basal systems. This crystal lattice rotation is the driver of softening. Fig. 12 shows the benchmark data that showcases the lattice reorientation behavior. We can see that as the axial strain increases, the crystal increasingly rotates towards the preferred
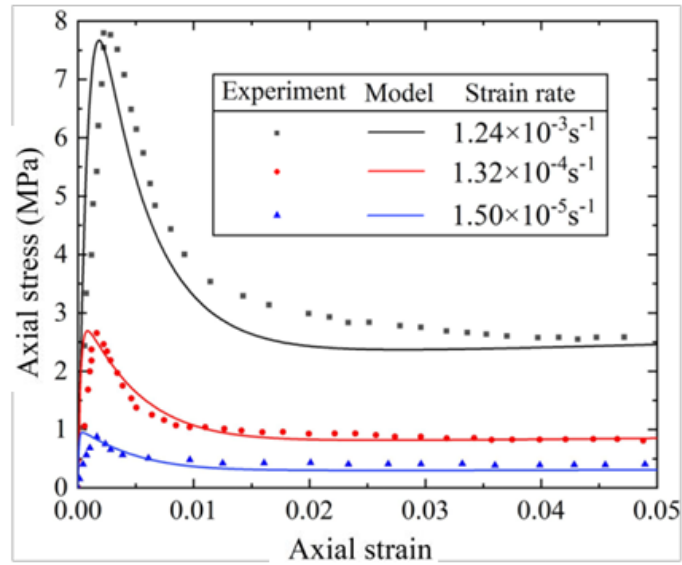
Figure 10: Benchmark and experimental stress-strain data for uniaxial compressions of Ih ice at various strain rates from [8].
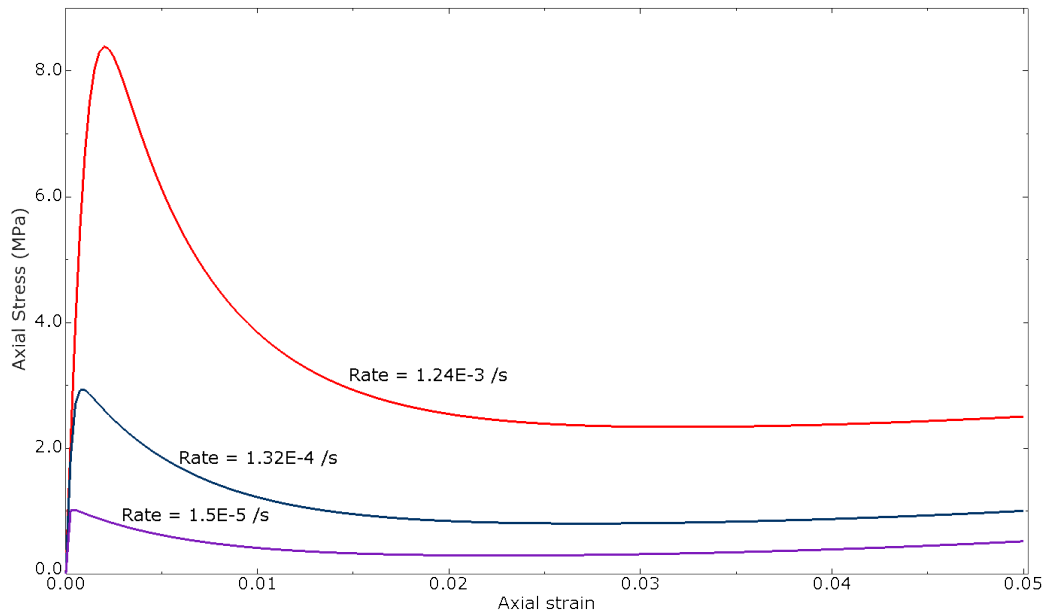

Figure 11: Stress-strain curves from model simulations for uniaxial compressions of Ih ice at various strain rates. The results show good agreement with the benchmark from Fig. 10.

14

basal systems. From Fig. 13, we can see that the proposed model can capture this behavior with very good accuracy ($< 5\%$ error in the predicted orientation) at all strains considered.
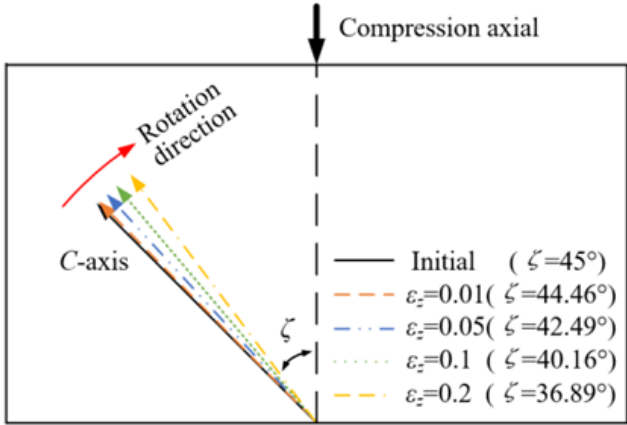

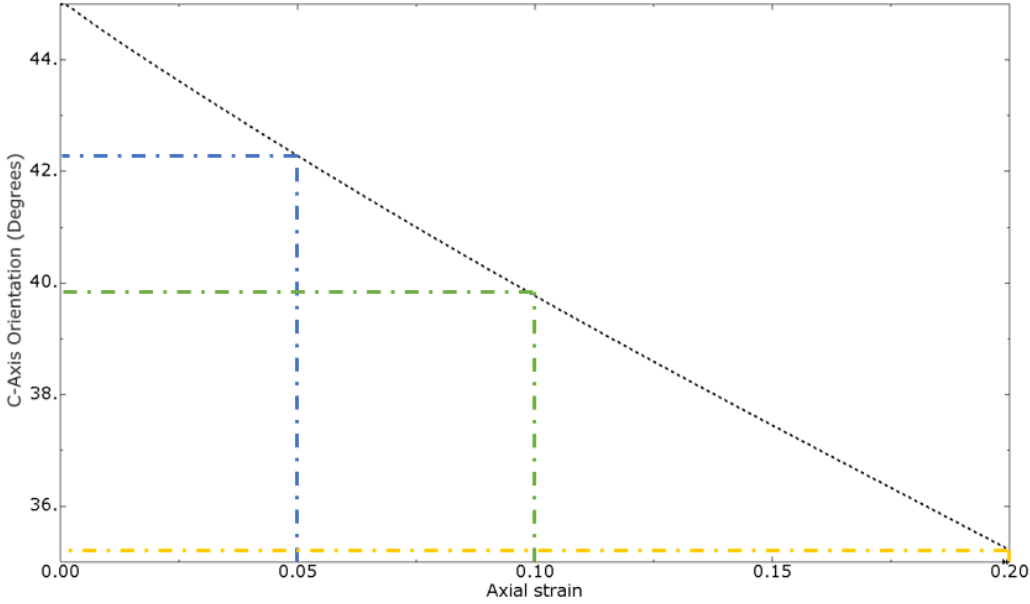Figure 12: Benchmark of the c-axis reorientation during uniaxial compression at 45° initial orientation from [8].

Figure 13: Results of the c-axis reorientation from model simulations starting at 45° initial orientation. The results show good agreement with the benchmark from Fig. 12.

5.3.3   Effect of c-axis orientation

Next, we look at the effect of crystal orientation on the stress-strain curve. From experimental evidence, we can see that ice shows no hardening or softening at a 0° c-axis orientation, strain hardening at a 90° c-axis orientation and strain softening at all other c-axis orientations. Fig. 14 shows the benchmark data for this behavior. Using our model, Fig. 15 shows that this behavior too can be captured since we can set different hardening and slip resistance parameters to different slip systems.
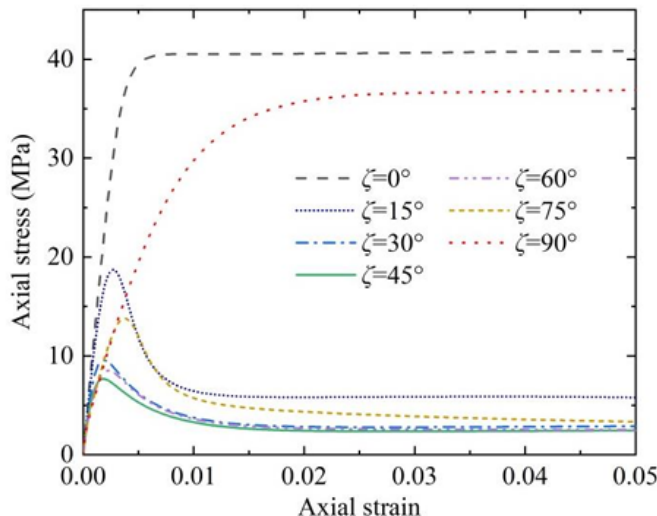

Figure 14: Benchmark of stress-strain data for uniaxial compressions of Ih ice at various c-axis orientations from [8].

5.3.4   Activation/ contribution of slip systems

Finally, we study the contribution of each slip system towards the total shear strain. From Fig. 16, we can see that at 0° c-axis orientation, the pyramidal slip system dominates since the other two systems are collinear with axial compression. At 90°, two of the three prismatic slip systems get activated, and are the dominant system of slip since they have lower resistance than the pyramidal systems. At all other orientations, the basal slip systems are activated, and are the dominant drivers of slip as they have the lowest slip resistance. Hence, at all other orientations, the crystal lattice rotates and reorients itself towards basal slip systems, leading to significant strain softening.
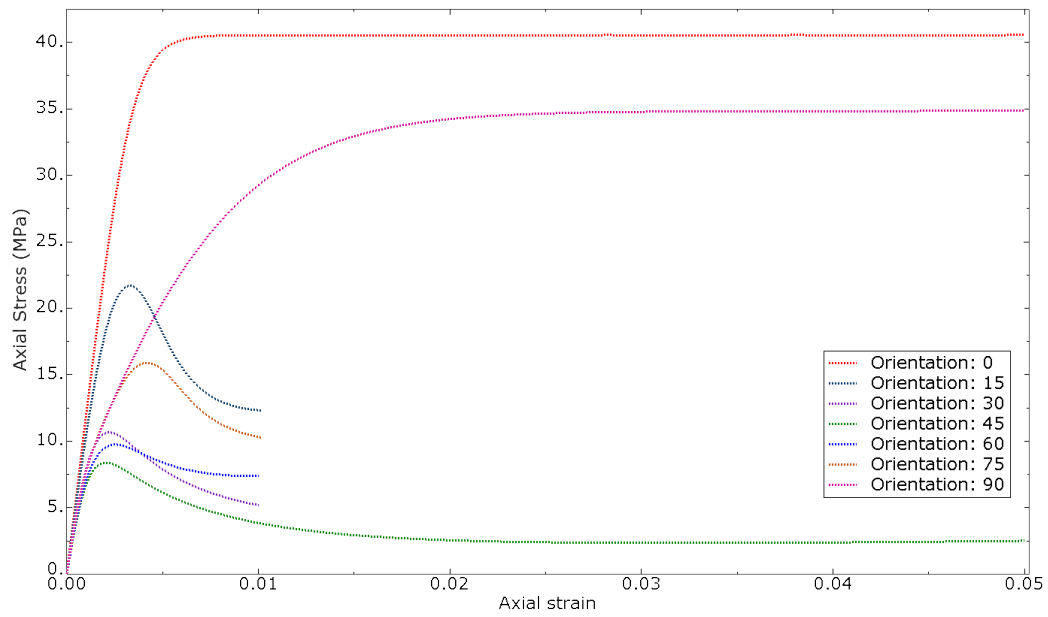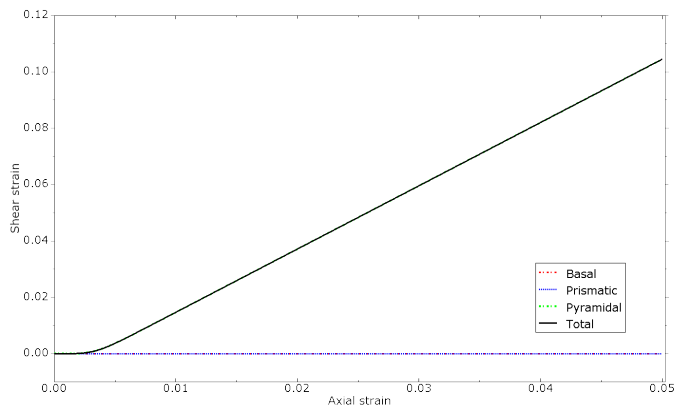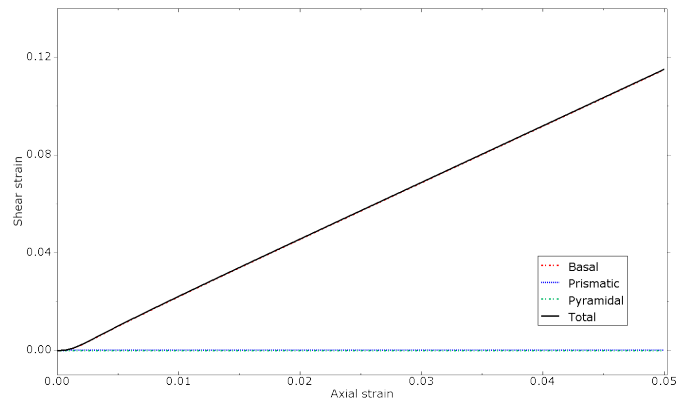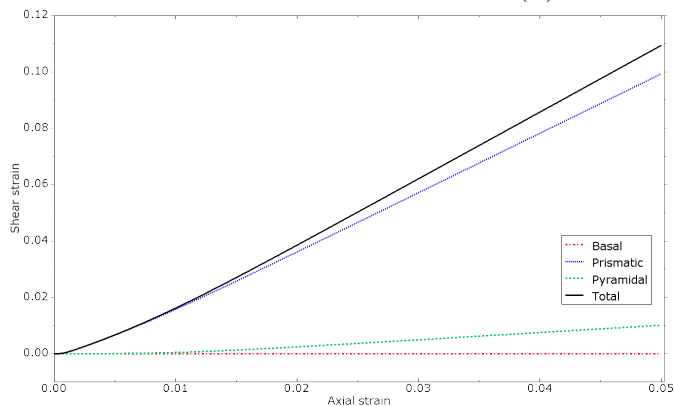
Figure 15: Stress-strain curves from model simulations for uniaxial compressions of Ih ice at various c-axis orientations. The results show good agreement with the benchmark from Fig. 14.

(a) c-axis orientation = 0°

(b) c-axis orientation = 45°

(c) c-axis orientation = 90°

Figure 16: Contribution of slips systems to total shear strain from model simulations at various c-axis orientations. Pyramidal systems dominate at 0°, prismatic systems dominate at 90°, and basal systems dominate at all other orientations.

18

5.3.5 Parameter identification strategy

Insights from the previous subsection provide a parameter-identification strategy. First, simulations can be carried out at 0^0 c-axis orientation since this isolates the pyramidal systems and the parameters can be tuned for pyramidal slip systems (no hardening). Next, simulations can be carried out at 90^0 c-axis orientation, and the prismatic slip system parameters can be tuned (shows strain hardening). Finally, another c-axis orientation can be set to identify the basal slip system parameters (with strain softening).

6 Conclusions

In this project, we successfully impelmented a rate-dependent crystal plasticity VUMAT for hexagonal close-packed (HCP) Ih ice, capturing the key deformation mechanisms observed experimentally. The proposed model accurately simulates the influence of strain rate on the deformation of ice as well as the role of c-axis orientation on axial compression behavior. Moreover, the model effectively incorporates the anisotropic behavior of Ih ice and the slip behavior and activation of basal, prismatic, and pyramidal systems.

Our findings demonstrate that basal slip systems dominate plastic deformation and shearing due to their low slip resistance, with lattice reorientation driving strain softening. The model also replicates stress-strain responses and slip system activations across a range of c-axis orientations, highlighting its accuracy.

7 Future Work

Future work would be on developing an interfacial model (with VUINTER) to model grain boundary sliding and other compressive fracture effects associated with polycrystalline ice [30]. Fig. 17 shows Coulombic shear fault and plastic shear fault in polycrystalline ice under natural light and polarized light. These models could also be extended to study large-scale sea ice floes after some regularization.
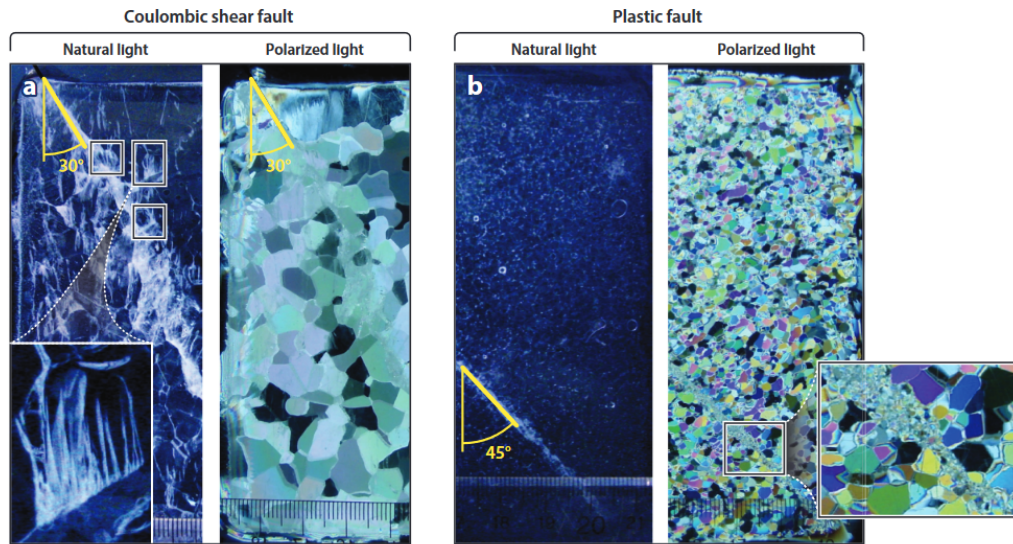
8 Acknowledgments

Figure 17: Coulombic shear fault and plastic shear fault in polycrystalline ice under natural light and polarized light. Source: [24]

References

[1] Christine Dianne Allan. *Plasticity of nickel base single crystal superalloys.* PhD thesis, Massachusetts Institute of Technology, 1995.

[2] Lallit Anand. Lecture notes of mit 2.073 solid mechanics: Plasticity and inelastic deformation.

[3] S Balasubramanian and L Anand. Plasticity of initially textured hexagonal polycrystals at high homologous temperatures: application to titanium. *Acta materialia*, 50(1):133–148, 2002.

[4] Srihari Balasubramanian. *Polycrystalline plasticity and its applications to deformation processing.* PhD thesis, Massachusetts Institute of Technology, 1995.

[5] Berill Blair, Malte Müller, Cyril Palerme, Rayne Blair, David Crookall, Maaike Knol-Kauffman, and Machiel Lamers. Coproducing sea ice predictions with stakeholders using simulation. *Weather, Climate, and Society*, 14(2):399–413, 2022.

[6] Curt A Bronkhorst, Surya R Kalidindi, and Lallit Anand. Polycrystalline plasticity and the evolution of crystallographic texture in fcc metals. *Philosophical Transactions of the Royal Society of London. Series A: Physical and Engineering Sciences*, 341(1662):443–477, 1992.

[7] David M Cole. Observations of pressure effects on the creep of ice single crystals. *Journal of Glaciology*, 42(140):169–175, 1996.

[8] Huiling Dai, Shaocheng Di, and Yanzhuo Xue. Crystal plasticity finite element modeling of elastic-viscoplastic deformation of ice single crystals. In *International Conference on Offshore Mechanics and Arctic Engineering*, volume 87844, page V006T07A022. American Society of Mechanical Engineers, 2024.

[9] Véronique Dansereau, Jérôme Weiss, Pierre Saramito, and Philippe Lattes. A maxwell elasto-brittle rheology for sea ice modelling. *The Cryosphere*, 10(3):1339–1359, 2016.

[10] GM Flato and WD Hibler. On a simple sea-ice dynamics model for climate studies. *Annals of Glaciology*, 14:72–77, 1990.

[11] PH Gammon, H Kiefte, and MJ Clouter. Elastic constants of ice by brillouin spectroscopy. *Journal of Glaciology*, 25(91):159–168, 1980.

[12] Kenneth M Golden, Luke G Bennetts, Elena Cherkaev, Ian Eisenman, Daniel Feltham, Christopher Horvat, Elizabeth Hunke, Christopher Jones, Donald K Perovich, Pedro Ponte-Castaneda, et al. Modeling sea ice. 2020.

[13] W DIII Hibler. A dynamic thermodynamic sea ice model. *Journal of physical oceanography*, 9(4):815–846, 1979.

[14] Surya R Kalidindi, Curt A Bronkhorst, and Lallit Anand. Crystallographic texture evolution in bulk deformation processing of fcc metals. *Journal of the Mechanics and Physics of Solids*, 40(3):537–569, 1992.

[15] Vladimir M Kattsov, Vladimir E Ryabinin, James E Overland, Mark C Serreze, Martin Visbeck, John E Walsh, Walt Meier, and Xiangdong Zhang. Arctic sea-ice change: a grand challenge of climate science. *Journal of Glaciology*, 56(200):1115–1121, 2010.

[16] NN Khusnatdinov and VF Petrenko. Fast-growth technique for ice single crystals. *Journal of crystal growth*, 163(4):420–425, 1996.

[17] Kenneth G Libbrecht. Physical dynamics of ice crystal growth. *Annual Review of Materials Research*, 47(1):271–295, 2017.

[18] Rebecca Lindsey and Michon Scott. Climate change: Arctic sea ice summer minimum. *Website: https://tinyurl. com/3x7knf28*, 2020.

[19] C Lobban, JL Finney, and WF Kuhs. The structure of a new phase of ice. *Nature*, 391(6664):268–270, 1998.

[20] James E Overland and Muyin Wang. When will the summer arctic be nearly sea ice free? *Geophysical Research Letters*, 40(10):2097–2101, 2013.

[21] Gleb Panteleev, Max Yaremchuk, Jacob N Stroh, Oceana P Francis, and Richard Allard. Parameter optimization in sea ice models with elastic–viscoplastic rheology. *The Cryosphere*, 14(12):4427–4451, 2020.

[22] CJ Readings and JT Bartlett. Slip in single crystals of ice. *Journal of Glaciology*, 7(51):479–491, 1968.

[23] Erland M Schulson. Brittle failure of ice. *Engineering fracture mechanics*, 68(17-18):1839–1887, 2001.

[24] Erland M Schulson and Carl E Renshaw. Fracture, friction, and permeability of ice. *Annual Review of Earth and Planetary Sciences*, 50(1):323–343, 2022.

[25] Frank Smith, Alexander Korobkin, Emilian Parau, Daniel Feltham, and Vernon Squire. Modelling of sea-ice phenomena, 2018.

[26] Scott R Stephenson and Rebecca Pincus. Challenges of sea-ice prediction for arctic marine policy and planning. *Journal of Borderlands Studies*, 33(2):255–272, 2018.

[27] Pierre Suquet, Hervé Moulinec, O Castelnau, Maurine Montagnat, Noël Lahellec, Fanny Grennerat, Paul Duval, and Renald Brenner. Multi-scale modeling of the mechanical behavior of polycrystalline ice under transient creep. *Procedia IUTAM*, 3:76–90, 2012.

[28] YL Trickett, I Baker, and PMS Pradhan. The orientation dependence of the strength of ice single crystals. *Journal of Glaciology*, 46(152):41–44, 2000.

[29] Johannes Weertman. Creep deformation of ice. *Annual Review of Earth and Planetary Sciences, Vol. 11, p. 215*, 11:215, 1983.

[30] YJ Wei and Lallit Anand. Grain-boundary sliding and separation in polycrystalline metals: application to nanocrystalline fcc metals. *Journal of the Mechanics and Physics of Solids*, 52(11):2587–2616, 2004.

[31] Jinlun Zhang and DA Rothrock. Effect of sea ice rheology in numerical investigations of climate. *Journal of Geophysical Research: Oceans*, 110(C8), 2005.